

Unconventional spectral signature of T_c in a pure d -wave superconductor

<https://doi.org/10.1038/s41586-021-04251-2>

Received: 2 August 2021

Accepted: 13 November 2021

Published online: 26 January 2022

 Check for updates

Su-Di Chen^{1,2,3,10,14}, Makoto Hashimoto^{4,14}, Yu He^{1,2,3,11}, Dongjoon Song^{5,12}, Jun-Feng He^{1,2,3,13}, Ying-Fei Li^{1,2,3}, Shigeyuki Ishida⁵, Hiroshi Eisaki⁵, Jan Zaanen⁶, Thomas P. Devereaux^{3,7}, Dung-Hai Lee^{8,9}, Dong-Hui Lu⁴ & Zhi-Xun Shen^{1,2,3}✉

In conventional superconductors, the phase transition into a zero-resistance and perfectly diamagnetic state is accompanied by a jump in the specific heat and the opening of a spectral gap¹. In the high-transition-temperature (high- T_c) cuprates, although the transport, magnetic and thermodynamic signatures of T_c have been known since the 1980s², the spectroscopic singularity associated with the transition remains unknown. Here we resolve this long-standing puzzle with a high-precision angle-resolved photoemission spectroscopy (ARPES) study on overdoped (Bi,Pb)₂Sr₂CaCu₂O_{8+δ} (Bi2212). We first probe the momentum-resolved electronic specific heat via spectroscopy and reproduce the specific heat peak at T_c , completing the missing link for a holistic description of superconductivity. Then, by studying the full momentum, energy and temperature evolution of the spectra, we reveal that this thermodynamic anomaly arises from the singular growth of in-gap spectral intensity across T_c . Furthermore, we observe that the temperature evolution of in-gap intensity is highly anisotropic in the momentum space, and the gap itself obeys both the d -wave functional form and particle–hole symmetry. These findings support the scenario that the superconducting transition is driven by phase fluctuations. They also serve as an anchor point for understanding the Fermi arc and pseudogap phenomena in underdoped cuprates.

The superconducting transition is one of the most studied phase transitions in condensed matter physics. In Bardeen–Cooper–Schrieffer (BCS) superconductors, this transition has four prominent signatures: the development of zero resistance, the onset of the Meissner effect, the peak of the electronic specific-heat coefficient $\gamma = C_e/T$ (where C_e is the electronic specific heat and T is the temperature), and the opening of the spectroscopic gap¹. In high- T_c cuprates, although the first three signatures are routinely observed, the gap is found to also exist in the resistive state^{3–9} and the spectroscopic singularity associated with T_c remains unclear^{6,9–12}. To resolve this puzzle, we carry out a high-precision photoemission study on Bi2212 single crystals. We focus on overdoped Bi2212 with T_c around 77 K (OD77; see Extended Data Fig. 1) to establish a clean case without interference from the pseudogap^{8,13–15}, additional orders¹⁶ and incoherent normal state⁸. For the ARPES measurements, both synchrotron-based and laser-based set-ups are used to access the entire Brillouin zone with optimized energy resolution; detector nonlinearity is carefully calibrated and corrected in a large dynamic range to ensure the accuracy of intensity measurements^{17,18}; and local heating manipulators are used to avoid

sample surface degradations in temperature scans^{6,8} (see Methods and Extended Data Fig. 2).

Thermodynamic signature from ARPES

We start by considering the connection between thermodynamics and spectroscopy. The specific heat coefficient γ , which peaks at T_c , is the temperature derivative of the entropy (S). For metals and superconductors in the noninteracting limit, $S = -k_B \int [f \ln f + (1-f) \ln(1-f)] \text{DOS}(E) dE$, where k_B is the Boltzmann constant, f is the Fermi function, and the quasiparticle density of states, $\text{DOS}(E)$, is equal to the momentum-integrated spectral function. In the cuprates, these relations are no longer exact owing to correlation effects. Nevertheless, in the less-correlated overdoped region⁸, one can obtain an approximate measure of DOS with momentum resolution using ARPES^{5,19}, from which the entropy can be estimated under the assumption that the superconducting phase fluctuations are much slower than the electronic response time (see Methods). Although more rigorous connections between the spectral function and thermodynamic quantities exist²⁰,

¹Department of Applied Physics, Stanford University, Stanford, CA, USA. ²Department of Physics, Stanford University, Stanford, CA, USA. ³Stanford Institute for Materials and Energy Sciences, SLAC National Accelerator Laboratory and Stanford University, Menlo Park, CA, USA. ⁴Stanford Synchrotron Radiation Lightsource, SLAC National Accelerator Laboratory, Menlo Park, CA, USA. ⁵National Institute of Advanced Industrial Science and Technology, Tsukuba, Japan. ⁶Institute Lorentz for Theoretical Physics, Leiden University, Leiden, The Netherlands. ⁷Department of Materials Science and Engineering, Stanford University, Stanford, CA, USA. ⁸Department of Physics, University of California, Berkeley, Berkeley, CA, USA. ⁹Materials Sciences Division, Lawrence Berkeley National Laboratory, Berkeley, CA, USA. ¹⁰Present address: Kavli Energy NanoScience Institute, University of California, Berkeley, Berkeley, CA, USA. ¹¹Present address: Department of Applied Physics, Yale University, New Haven, CT, USA. ¹²Present address: Center for Correlated Electron Systems, Institute for Basic Science, Seoul, Republic of Korea. ¹³Present address: Department of Physics, University of Science and Technology of China, Hefei, China. ¹⁴These authors contributed equally: Su-Di Chen, Makoto Hashimoto. ✉e-mail: zxshen@stanford.edu

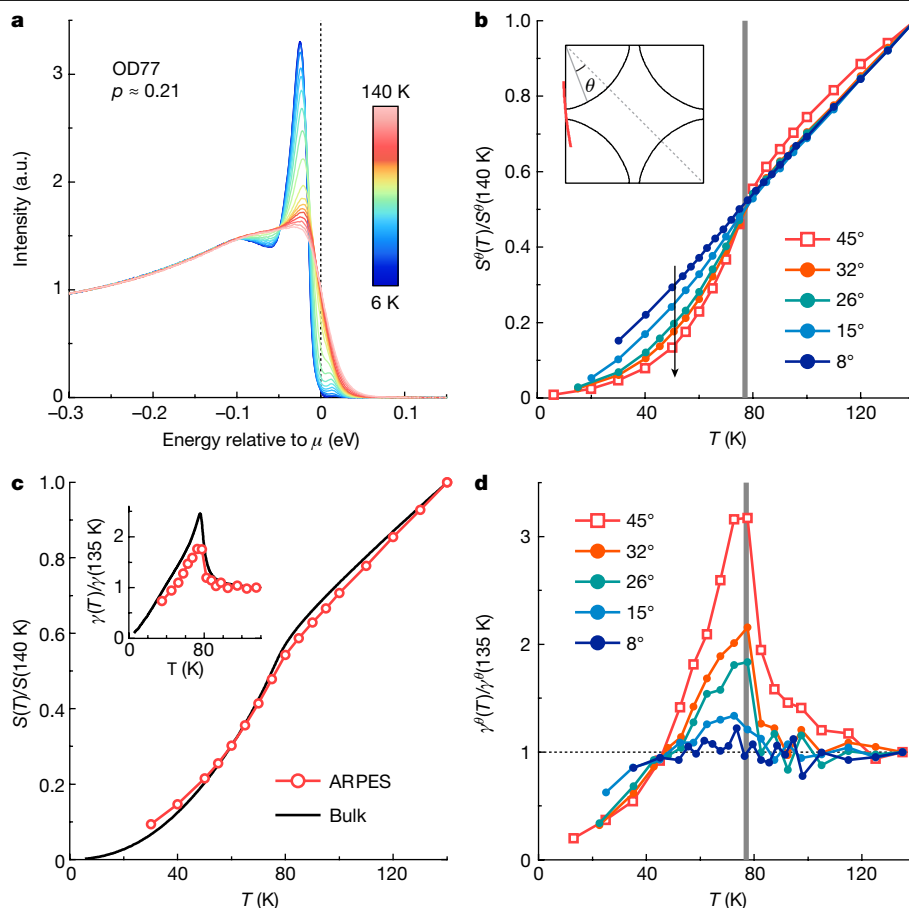


Fig. 1 | Momentum-resolved specific heat from ARPES. **a**, ARPES energy distribution curves (EDCs) near the chemical potential (μ) integrated along the momentum cut marked in **b**, inset (red). The experimental condition is optimized to mainly probe the antibonding band. Data from different temperatures are normalized such that the average intensity within $[-0.3, -0.25]$ eV equals 1. OD77, overdoped Bi2212 with $T_c \approx 77$ K and doping $p \approx 0.21$. **b**, Temperature evolutions of electronic entropy (S) at various Fermi surface angles, calculated using EDCs integrated along line cuts that cross the Fermi surface at different momenta. The black arrow marks the entropy

reduction due to superconductivity. The inset shows the schematic Fermi surface from the antibonding band in the first Brillouin zone and the definition of the Fermi surface angle θ . **c**, Temperature dependence of S from the antibonding band summed over the first Brillouin zone (see Methods). Also plotted is the previous bulk result on overdoped Bi2212 with T_c around 76 K (ref. ¹⁴). Inset, the specific heat coefficient γ obtained as the numerical derivative of S plotted together with the bulk result. **d**, Temperature evolution of γ at different Fermi surface angles obtained using curves in **b**. The grey vertical lines in **b** and **d** mark the T_c determined by magnetic susceptibility measurements.

they cannot be used here without a priori knowledge of bare band dispersions.

In Fig. 1a, we plot the ARPES energy distribution curves (EDCs) integrated along the Brillouin zone boundary at various temperatures. The experimental condition is optimized such that the intensity is predominantly contributed by the antibonding band. Since these EDCs correspond to the product of f and the antinodal DOS, we multiply each of them by $-k_B[f \ln f + (1-f) \ln(1-f)]/f$ and integrate over energy to obtain the antinodal S up to a temperature-independent factor related to the photoemission matrix element. The same procedure is repeated for several Fermi surface angles (θ), and the results are shown in Fig. 1b. As marked by the grey arrow, the entropy reduction from superconductivity is clearly observed. The effect is stronger for larger θ , reflecting the d -wave gap form. Using the ARPES-derived tight-binding bandstructure and scattering rate, we further perform a Brillouin zone summation and obtain the temperature evolution of entropy for the entire antibonding band (see Methods and Extended Data Figs. 3, 4). As shown in Fig. 1c, the result qualitatively agrees with that from previous bulk measurements¹⁴.

We calculate γ as the numerical derivative of each S curve. The γ summed over the Brillouin zone features a prominent peak (Fig. 1c, inset), reflecting the thermodynamic anomaly associated with the

superconducting phase transition. Compared with the bulk result, the peak from spectroscopy normalized to its high-temperature value has a similar width but a smaller height, which might be caused by interaction effects such as the temperature-dependent mass renormalization from electron–phonon coupling²¹. The momentum dependence of $\gamma/\gamma(135$ K) is shown in Fig. 1d, where for larger θ we find higher peaks at T_c and smaller values at low temperature. These observations are consistent with the anisotropic gap form: because the gap size is maximized at $\theta = 45^\circ$, the antinodal electrons should have the strongest effect on the energetics of the superconducting transition while contributing the least to the low-temperature quasiparticle excitations.

Spectroscopic singularity across T_c

To understand the microscopic origin of the thermodynamic anomaly at T_c , we examine the full information provided by ARPES. In Fig. 2a, b, we show two representative ARPES spectra taken along the Brillouin zone boundary, where the continuous and gapped dispersions from the antibonding band are clearly observed at 140 K and 85 K, respectively. From these images, the gap size (on the occupied side; see Extended Data Fig. 5 for details) and the momentum-integrated zero-energy intensity (A_0 , see also Fig. 2c) are extracted and plotted in Fig. 2d. With

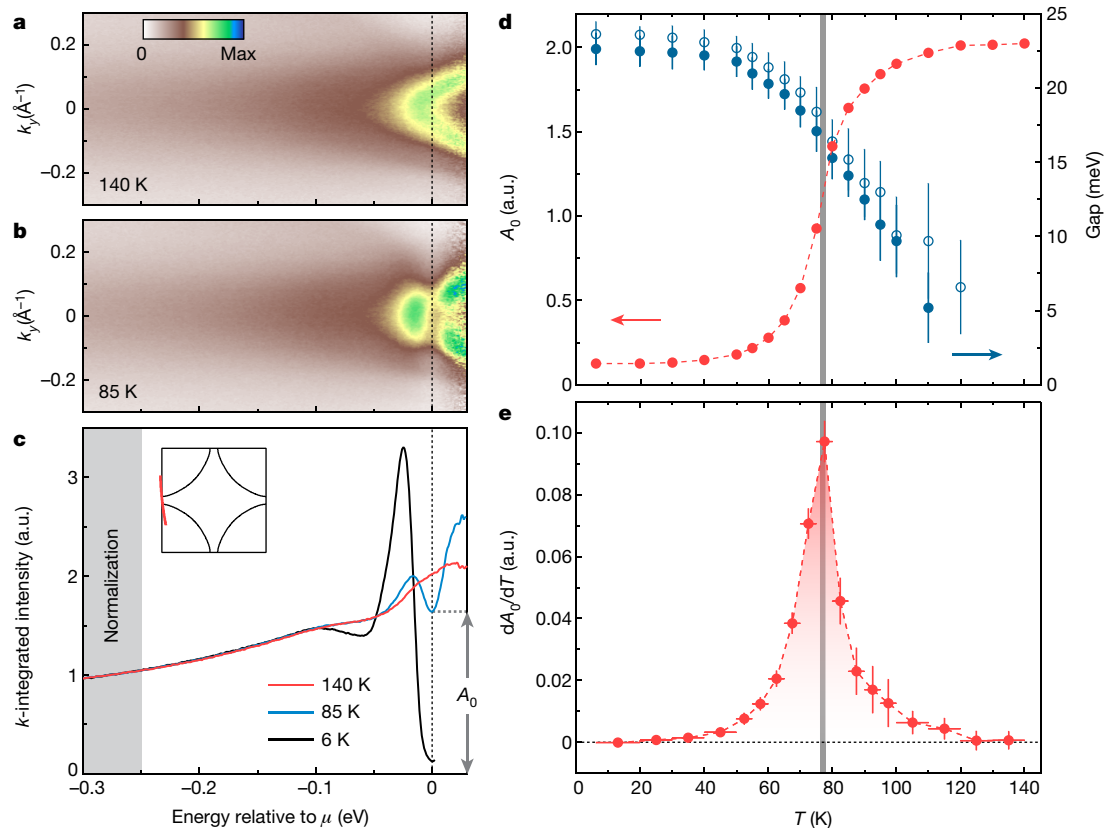


Fig. 2 | Spectroscopic signature of T_c . **a, b**, ARPES spectra at 140 K (**a**) and 85 K (**b**) along the momentum trajectory marked in **c**, inset (red). The intensity is divided by the resolution-convolved Fermi function. **c**, EDCs at selected temperatures integrated along the momentum trajectory marked in the inset. The curves are normalized such that the average intensity between $[-0.3, -0.25]$ eV is 1. **d**, Red circles show the momentum-integrated intensity at zero energy (A_0 as defined in **c**) as a function of temperature. Solid and open

blue circles represent the antinodal gap sizes obtained using the Fermi-momentum (k_F) EDCs from the $k_y > 0$ and $k_y < 0$ sides, respectively. The error bars reflect 3σ errors from data noise and chemical potential determination. **e**, Temperature derivative of A_0 obtained numerically using the data in **d**. Vertical error bars are from A_0 uncertainties and horizontal error bars reflect the temperature step size. The grey vertical lines in **d** and **e** mark the T_c determined by magnetic susceptibility measurements. a.u., arbitrary units.

increasing temperature across T_c , we find a gradual reduction in gap size and a rapid growth in A_0 . Yet the most singular behaviour exists in the temperature derivative of A_0 , where a sharp peak is found to coincide with T_c (Fig. 2e). Since γ scales with the sum of the low-energy DOS and its temperature derivative multiplied by temperature, the singular gap-filling rate dA_0/dT observed here is essentially responsible for the γ peak at T_c .

We apply a similar analysis to data from different momentum cuts. The gap sizes at different momenta and temperatures are plotted in Fig. 3a. It should be noted that the gap cannot be reliably determined if the quasiparticle peak width exceeds the gap size. Therefore, for each momentum with increasing temperature, we stop the gap analysis once this unreliable condition is reached (see also Extended Data Fig. 5). After normalizing all the data points by their corresponding d -wave form factors $|\cos k_x - \cos k_y|/2$, we find that they collapse into a single curve for $T < T_c$, whereas the spread for $T > T_c$ is within experimental error (Fig. 3b). This indicates that d -wave gap form is preserved at least up to T_c .

The temperature dependence of A_0 at various Fermi surface angles is shown in Fig. 3c, where a strong momentum anisotropy is observed. For $\theta = 45^\circ$, A_0 has a small residual at low temperature and grows to around half of the normal-state value at T_c . By contrast, near the node, the low-temperature residual is much higher, and the intensity recovery is almost complete at T_c . The same anisotropy is manifested in the dA_0/dT curves. Although the peak always aligns with T_c within experimental error, both the peak height and the above- T_c peak weight become smaller for momentum cuts closer to the node. To confirm that this

anisotropy is not an artefact caused by finite energy resolution, we intentionally broaden the ARPES spectra such that every momentum cut has the same resolution-to-gap ratio and then repeat the analysis. We find negligible difference between the results without and with intentional broadening (Extended Data Fig. 6), which indicates that the momentum dependence is intrinsic.

Pure superconducting gap above T_c

The anisotropic gap-filling behaviour in Fig. 3c bears some resemblance to the Fermi arc and pseudogap phenomena observed in the underdoped cuprates, the origins of which are heavily debated, largely because of the coexistence of various orders and fluctuations^{3,16,22}. Here, to establish a clean baseline in the overdoped, relatively simple region of the phase diagram, we further examine the character of the gap above T_c to clarify its origin. The momentum and temperature evolution of the spectra is shown in Fig. 4a. Consistent with Fig. 3c, we find that the intensity suppression caused by the gap persists to higher temperatures for momentum cuts closer to the antinode. On the other hand, the data show that the gap is always centred at the chemical potential regardless of momentum and temperature. In Fig. 4b, we plot the dispersion branches above and below the chemical potential near the gapped Fermi surface above T_c at 85 K (see Extended Data Fig. 7 for details), from which the gap centre is quantitatively determined. The accurate alignment between the gap centre and chemical potential reflects the particle-hole symmetry of the gap. This symmetry is intrinsic to the Bogoliubov quasiparticle dispersions in superconductors but

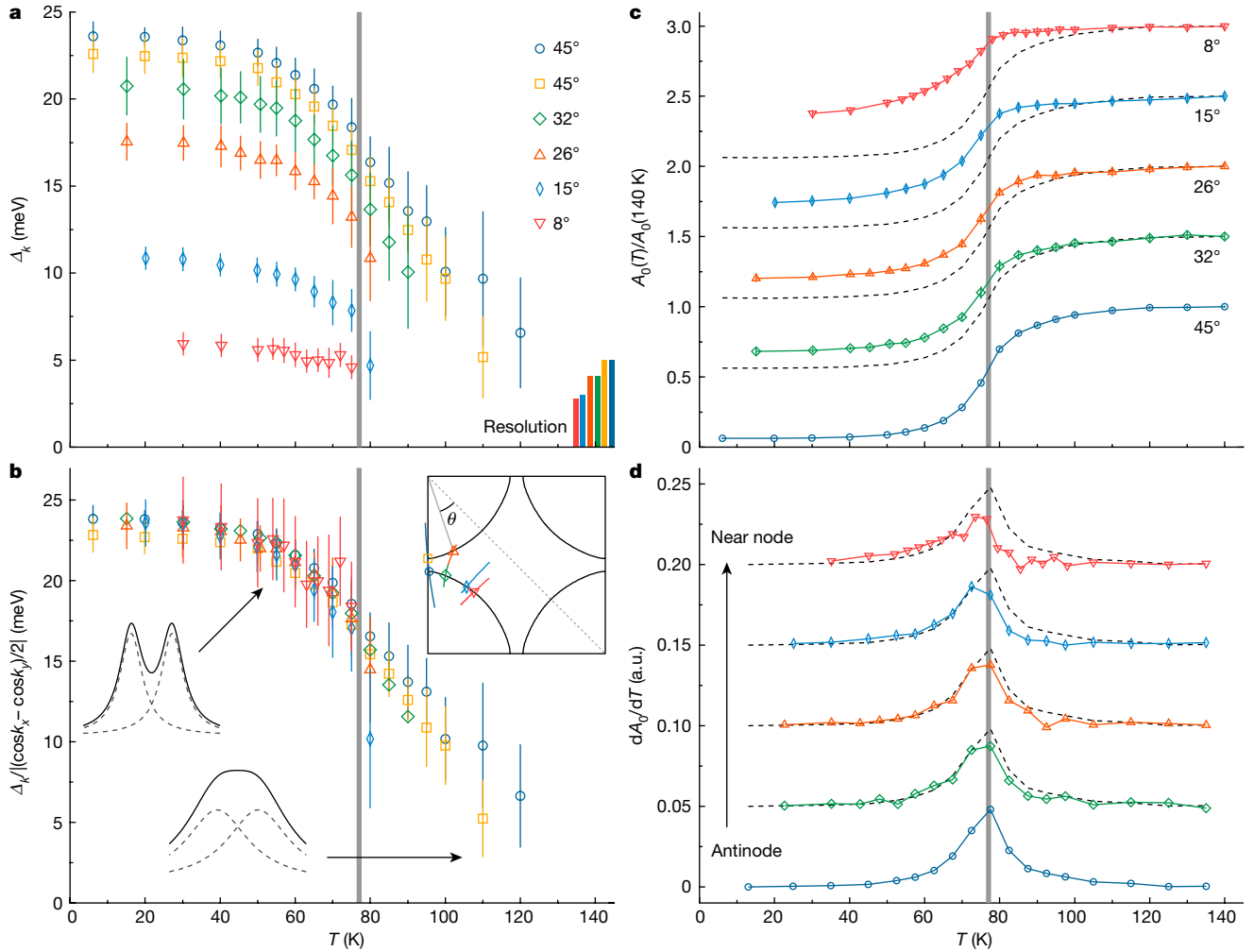


Fig. 3 | Momentum dependence of gap and in-gap intensity. **a**, Temperature evolution of gap sizes obtained from k_F EDCs at momentum points marked in the top-right inset in **b**. The corresponding Fermi surface angles are labelled. The energy resolution for each measurement is represented by the vertical bar on the lower right corner with the same colour. The error bars reflect 3σ errors from data noise and chemical potential determination. **b**, As in **a**, with the gap sizes divided by their corresponding d -wave form factors. The middle inset shows the schematic lineshape of k_F EDCs from which the gap sizes can be extracted. The bottom inset illustrates that such extraction is no longer

incompatible with density-wave or magnetic-order-induced gaps given the Fermi surface shape of Bi2212. Thus, our observations indicate that the gap has a pure superconducting character.

Discussion

The order parameter of a superconductor has an amplitude and a phase. Our observation of a pure superconducting gap in the normal state directly demonstrates that the amplitude does not vanish above T_c , consistent with the interpretations from several earlier ARPES studies^{4–6,8,9}. This leaves phase fluctuations as the leading candidate²³ for driving the superconducting transition, a scenario also suggested by previous bulk measurements^{24–27} on several cuprate systems. Here we further consider the behaviour of A_0 in the presence of phase fluctuations (see also Extended Data Fig. 8). With a constant gap amplitude, it has been shown that the in-gap spectral weight increases with fluctuations in the phase configuration²⁸. Moreover, because of the d -wave gap form and the anisotropic bandstructure in the cuprates, the same amount of phase fluctuations is expected to produce a higher gap filling for

reliable if the peak width is larger than the gap size. **c**, Momentum-integrated zero-energy intensity A_0 from different Fermi surface angles. Curves are offset in steps of 0.5 for clarity. Replicas of the antinodal curve at $\theta = 45^\circ$ are plotted in grey for better comparison. The momentum trajectories for integration are marked in the top-right inset in **b** using the corresponding colours. The error bars reflect 3σ errors from data noise and chemical potential determination. **d**, Numerical derivatives of the data in **c**. The vertical grey line in each panel marks T_c .

momentum closer to the node^{29,30}. Thus, the phase fluctuation scenario qualitatively explains the singular and anisotropic change of A_0 across T_c observed in our experiments.

Another important feature in our data is the residual A_0 at low temperature. Near the antinode, the residual is only around 6% of the normal-state value, which gives an upper bound for the area percentage of metallic domains in the ground state. On the other hand, the ratio increases substantially towards the node, reaching around 38% at a Fermi surface angle of 8° ($|\cos k_x - \cos k_y|/2 \approx 0.25$). This suggests a moderate level of disorder in the system, which is expected to contribute to the reduction of the superconducting phase stiffness^{31,32}. This effect may act cooperatively with the sign change in the order parameter, the low-energy Van Hove singularity⁹, and the low dimensionality of the system^{33,34} to create a clear separation between the gap closing and phase coherence temperatures. Regardless of the details, the data we report here emphasize the critical role of phase fluctuations and stipulate the crucial momentum-resolved spectroscopic fingerprint for the quantitative understanding of overdoped cuprates.

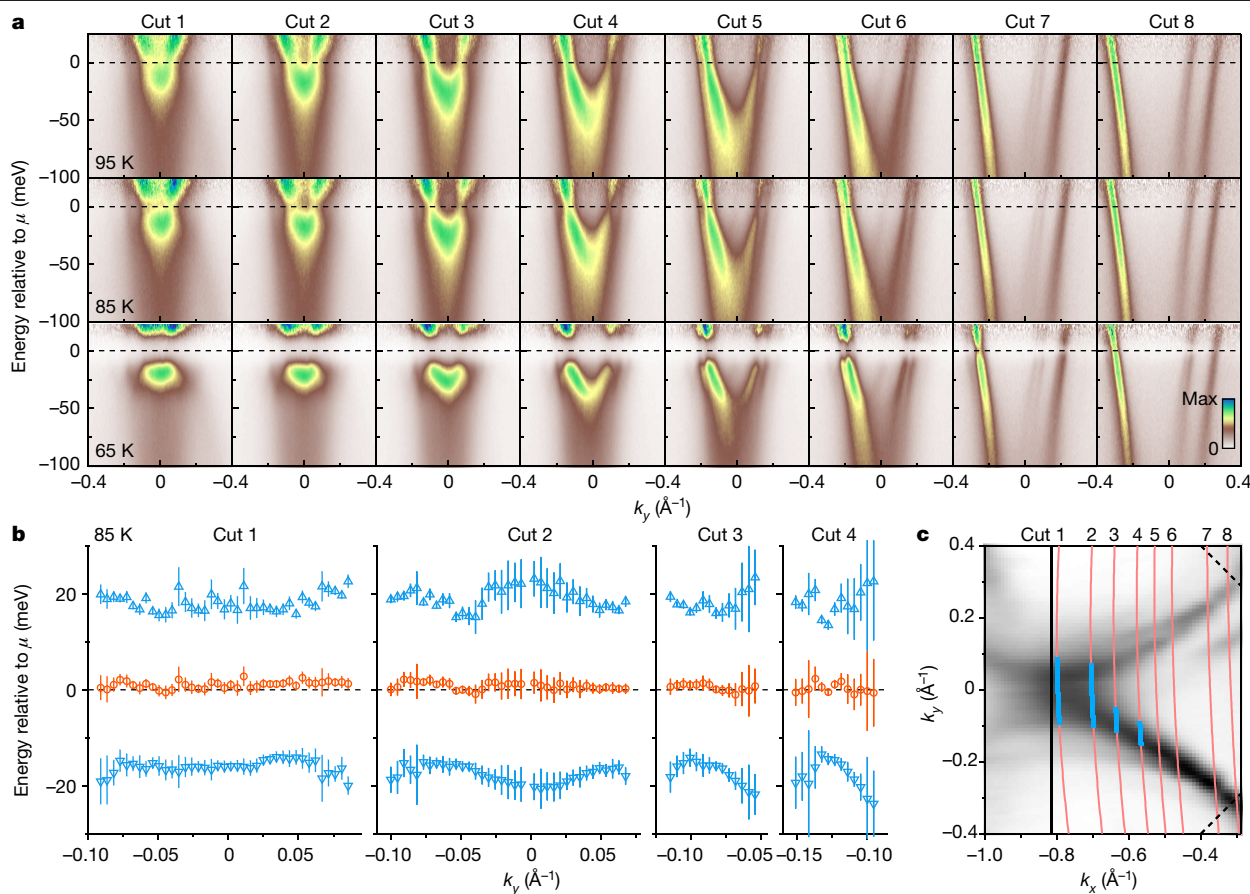


Fig. 4 | Particle-hole symmetry of the gap. **a**, ARPES energy-momentum cuts at 95 K (top row), 85 K (middle row), and 65 K (bottom row). The corresponding momentum trajectory for each column is labelled in **c** (pink). The intensity is divided by the resolution-convolved Fermi function. The weak dispersions most visible in the last two columns are caused by superstructures. **b**, Upper and lower dispersion branches (blue triangles) and their centres (orange circles) at 85 K along the momentum trajectories marked in blue in **c**. Because of the lower signal-to-noise ratio above the chemical potential, the dispersions

are obtained by fitting each Fermi-function-divided EDC using two Lorentzian peaks with identical width plus a constant background. The error bars reflect 3σ errors from fitting and chemical potential determination. **c**, ARPES intensity integrated over the energy window $[-15, 15]$ meV at 60 K. The solid and dashed black lines mark the Brillouin zone boundary and diagonal, respectively. The pink and blue curves mark the momentum locations for data in **a** and **b**, respectively.

To summarize, using high-precision ARPES measurements, we have uncovered the spectroscopic signature of the superconducting transition which has eluded detection despite decades of efforts following the discovery of the normal-state gap. Our observations unify the spectroscopic and thermodynamic results in cuprate superconductors and establish a microscopic paradigm for the specific heat of a d -wave superconductor with strong phase fluctuations. The methodology developed here may also be used to study phase transitions and correlation effects in other novel systems.

Online content

Any methods, additional references, Nature Research reporting summaries, source data, extended data, supplementary information, acknowledgements, peer review information; details of author contributions and competing interests; and statements of data and code availability are available at <https://doi.org/10.1038/s41586-021-04251-2>.

1. Tinkham, M. *Introduction to Superconductivity* (Dover, 2004).
2. Schrieffer, J. R. & Brooks, J. S. *Handbook of High-Temperature Superconductivity: Theory and Experiment* (Springer, 2007).
3. Damascelli, A., Hussain, Z. & Shen, Z.-X. Angle-resolved photoemission studies of the cuprate superconductors. *Rev. Mod. Phys.* **75**, 473–541 (2003).
4. Kondo, T. et al. Disentangling Cooper-pair formation above the transition temperature from the pseudogap state in the cuprates. *Nat. Phys.* **7**, 21–25 (2011).

5. Reber, T. J. et al. The origin and non-quasiparticle nature of Fermi arcs in $\text{Bi}_2\text{Sr}_2\text{CaCu}_2\text{O}_{8-\delta}$. *Nat. Phys.* **8**, 606–610 (2012).
6. Kondo, T. et al. Point nodes persisting far beyond T_c in $\text{Bi}2212$. *Nat. Commun.* **6**, 7699 (2015).
7. Zaki, N. et al. Cuprate phase diagram and the influence of nanoscale inhomogeneities. *Phys. Rev. B* **96**, 195163 (2017).
8. Chen, S.-D. et al. Incoherent strange metal sharply bounded by a critical doping in $\text{Bi}2212$. *Science* **366**, 1099–1102 (2019).
9. He, Y. et al. Superconducting fluctuations in overdoped $\text{Bi}_2\text{Sr}_2\text{CaCu}_2\text{O}_{8-\delta}$. *Phys. Rev. X* **11**, 031068 (2021).
10. Hashimoto, M. et al. Direct spectroscopic evidence for phase competition between the pseudogap and superconductivity in $\text{Bi}_2\text{Sr}_2\text{CaCu}_2\text{O}_{8-\delta}$. *Nat. Mater.* **14**, 37–42 (2014).
11. Reber, T. J. et al. Pairing, pair-breaking, and their roles in setting the T_c of cuprate high temperature superconductors. Preprint at <https://arxiv.org/abs/1508.06252> (2015).
12. Gomes, K. K. et al. Visualizing pair formation on the atomic scale in the high- T_c superconductor $\text{Bi}_2\text{Sr}_2\text{CaCu}_2\text{O}_{8-\delta}$. *Nature* **447**, 569–572 (2007).
13. Timusk, T. & Statt, B. The pseudogap in high-temperature superconductors: an experimental survey. *Reports Prog. Phys.* **62**, 61–122 (1999).
14. Loram, J. W., Luo, J., Cooper, J. R., Liang, W. Y. & Tallon, J. L. Evidence on the pseudogap and condensate from the electronic specific heat. *J. Phys. Chem. Solids* **62**, 59–64 (2001).
15. Tallon, J. L., Storey, J. G., Cooper, J. R. & Loram, J. W. Locating the pseudogap closing point in cuprate superconductors: absence of entrant or reentrant behavior. *Phys. Rev. B* **101**, 174512 (2020).
16. Keimer, B., Kivelson, S. A., Norman, M. R., Uchida, S. & Zaanen, J. From quantum matter to high-temperature superconductivity in copper oxides. *Nature* **518**, 179–186 (2015).
17. Mannella, N. et al. Correction of non-linearity effects in detectors for electron spectroscopy. *J. Electron Spectrosc.* **141**, 45–59 (2004).
18. Reber, T. J., Plumb, N. C., Waugh, J. A. & Dessau, D. S. Effects, determination, and correction of count rate nonlinearity in multi-channel analog electron detectors. *Rev. Sci. Instrum.* **85**, 043907 (2014).
19. Kondo, T. et al. Formation of gapless Fermi arcs and fingerprints of order in the pseudogap state of cuprate superconductors. *Phys. Rev. Lett.* **111**, 157003 (2013).

20. Norman, M. R., Randeria, M., Jankó, B. & Campuzano, J. C. Condensation energy and spectral functions in high-temperature superconductors. *Phys. Rev. B* **61**, 14742 (2000).
21. Cuk, T. et al. Coupling of the B_{1g} phonon to the antinodal electronic states of $\text{Bi}_2\text{Sr}_2\text{Ca}_{0.92}\text{Y}_{0.08}\text{Cu}_2\text{O}_{8+\delta}$. *Phys. Rev. Lett.* **93**, 117003 (2004).
22. Sobota, J. A., He, Y. & Shen, Z.-X. Angle-resolved photoemission studies of quantum materials. *Rev. Mod. Phys.* **93**, 025006 (2021).
23. Emery, V. J. & Kivelson, S. A. Importance of phase fluctuations in superconductors with small superfluid density. *Nature* **374**, 434–437 (1995).
24. Wang, Y. et al. Field-enhanced diamagnetism in the pseudogap state of the cuprate $\text{Bi}_2\text{Sr}_2\text{CaCu}_2\text{O}_{8+\delta}$ superconductor in an intense magnetic field. *Phys. Rev. Lett.* **95**, 247002 (2005).
25. Li, L. et al. Diamagnetism and Cooper pairing above T_c in cuprates. *Phys. Rev. B* **81**, 054510 (2010).
26. Uemura, Y. J. et al. Magnetic-field penetration depth in $\text{Ti}_2\text{Ba}_2\text{CuO}_{6+\delta}$ in the overdoped regime. *Nature* **364**, 605–607 (1993).
27. Božović, I., He, X., Wu, J. & Bollinger, A. T. Dependence of the critical temperature in overdoped copper oxides on superfluid density. *Nature* **536**, 309–311 (2016).
28. Eckl, T., Scalapino, D. J., Arrigoni, E. & Hanke, W. Pair phase fluctuations and the pseudogap. *Phys. Rev. B* **66**, 140510 (2002).
29. Franz, M. & Millis, A. J. Phase fluctuations and spectral properties of underdoped cuprates. *Phys. Rev. B* **58**, 14572–14580 (1998).
30. Berg, E. & Altman, E. Evolution of the Fermi surface of d -wave superconductors in the presence of thermal phase fluctuations. *Phys. Rev. Lett.* **99**, 247001 (2007).
31. Lee-Hone, N. R., Dodge, J. S. & Broun, D. M. Disorder and superfluid density in overdoped cuprate superconductors. *Phys. Rev. B* **96**, 024501 (2017).
32. Li, Z.-X., Kivelson, S. A. & Lee, D.-H. Superconductor-to-metal transition in overdoped cuprates. *npj Quantum Mater.* **6**, 36 (2021).
33. Kosterlitz, J. M. & Thouless, D. J. Ordering, metastability and phase transitions in two-dimensional systems. *J. Phys. C* **6**, 1181–1203 (1973).
34. Janke, W. & Matsui, T. Crossover in the XY model from three to two dimensions. *Phys. Rev. B* **42**, 10673–10681 (1990).

Publisher's note Springer Nature remains neutral with regard to jurisdictional claims in published maps and institutional affiliations.

© The Author(s), under exclusive licence to Springer Nature Limited 2022

Methods

Sample and measurement

We studied overdoped Bi2212 samples with T_c around 77 K (OD77). Single crystals with a nominal composition of $\text{Bi}_{1.41}\text{Pb}_{0.66}\text{Sr}_{1.95}\text{CaCu}_2\text{O}_{8+\delta}$ were grown by the floating-zone (FZ) method. We annealed the crystals at 550 °C in a gas mixture of 3% O_2 and 97% N_2 for 40 h or longer to obtain OD77 samples. The gas pressure was kept at 1 atm during the annealing process. We also annealed additional crystals from the same FZ growth batch in pure N_2 at 595 °C and found their T_c to be around 95 K. This provides a lower bound for the optimal T_c ($T_{c,\text{max}}$) of this FZ batch. Taking the upper bound of $T_{c,\text{max}}$ to be 98 K, which is to our best knowledge the highest T_c reported in single-crystalline Bi2212¹⁰, we determine the nominal doping (p) of the OD77 samples to be 0.210(2) using the empirical parabolic relation³⁵, $T_c = T_{c,\text{max}} \times [1 - 82.6 \times (p - 0.16)^2]$.

Synchrotron and laser ARPES measurements were performed at beamline 5-4 of the Stanford Synchrotron Radiation Lightsource and at the Shen laboratory at Stanford University, using 19-eV and 7-eV photons, respectively. Both photon energies highlight the antibonding band in Bi2212. For the synchrotron measurements, a hemispherical electron analyser (R4000, Scienta) was used, and the analyser slit was parallel to the Cu–O bond direction and perpendicular to the photon polarization. For the laser measurements, a similar analyser (R8000, Scienta) was used, and the linear light polarization was rotated at the beginning of each experiment to maximize the signal-to-background ratio. The detector nonlinearity was calibrated and corrected^{17,18,36}. The chemical potential of the sample and the energy resolution of the system were determined by fitting the Fermi edge of polycrystalline gold with space-charge effects calibrated and taken into account³⁶. An energy-independent background was determined using intensity far above the chemical potential and subtracted from the data. For the synchrotron set-up, a weak photon sideband from grating imperfections (<4% of total flux) was also calibrated using the gold Fermi edge and the sideband contribution to the photoemission intensity was removed³⁶.

In each experiment, the sample was first transferred onto a cryogenic manipulator which can travel between an upper chamber and a lower chamber. It was then cleaved between 50 K and 60 K in the upper chamber and moved to the lower chamber for measurement within 10 min. Once the sample was cleaved, the vacuum was kept at better than 2×10^{-11} (3×10^{-11}) torr in the measurement chamber and better than 3×10^{-11} (7×10^{-11}) torr in the upper chamber for the synchrotron (laser) experiments at all times. We expect the actual vacuum near the sample surface to be even higher because of the cryopumping effect from the manipulator radiation shield.

To avoid ageing, the total measurement time was limited to around 24 h for each freshly cleaved surface. Within 24 h, we can measure either a single energy-momentum cut with dense temperature steps or a set of cuts at selected temperatures. As a result, the data presented were collected in five separate experiments. All measurements above 60 K were completed using the local heating method with thermal cycling for consistency checks. All measurements below 60 K were done either with decreasing temperature only to minimize outgassing or with thermal cycling. The details for each experiment are provided in Extended Data Table 1. The thermal cycling data are plotted in Extended Data Fig. 2.

After each ARPES experiment, a thin piece of crystal was exfoliated from the cleaved surface using Kapton tapes. The magnetic susceptibility of this thin piece was then measured using the a.c. magnetic susceptibility module of a physical property measurement system (Quantum Design). The excitation field was roughly perpendicular to the CuO_2 plane, and the field frequency was 4 kHz. The real part of the a.c. susceptibility (χ') is plotted in Extended Data Fig. 1. We noticed that for thin crystals, an excitation field of a few oersteds can already broaden the transition (Extended Data Fig. 1e), probably because of

the inhomogeneous field distribution near the sample edge. Thus, the data in Extended Data Fig. 1a–e provide upper bounds for the superconducting transition width. On the other hand, the transition was found to be very sharp in thick crystals (Extended Data Fig. 1f), indicating high sample quality.

Details of momentum summation for entropy

The total entropy of the antibonding band is given by $S(T) = \int [S^\theta(T)/S^\theta(140\text{ K})] S^\theta(140\text{ K}) d\theta$. We obtain $S^\theta(T)/S^\theta(140\text{ K})$ using data in Fig. 1b via linear interpolation and the results are plotted in Extended Data Fig. 3a. We then calculate $S^\theta(140\text{ K})$ using $S^\theta(140\text{ K}) = -k_B [f \ln f + (1-f) \ln(1-f)] A^\theta(E) dE$, where $A^\theta(E)$ is the spectral function $A(k, E)$ integrated between Fermi surface angles θ and $\theta + d\theta$ (blue region in Extended Data Fig. 3c inset), and $A(k, E) = \Gamma_{140\text{ K}} / \{\pi[(E - \varepsilon_k)^2 + \Gamma_{140\text{ K}}^2]\}$. Here $\varepsilon_k = -2t_0(\cos k_x + \cos k_y) - 4t_1 \cos k_x \cos k_y - \mu$ and the ARPES-derived tight-binding parameters are $t_0 = 0.166$, $t_1 = -0.0544$, and $\mu = -0.2055$ in units of eV (see Extended Data Fig. 4 for details). $\Gamma_{140\text{ K}}$ is the energy-independent scattering rate, which we found to be around 35 meV for the antinodal data at 140 K. We perform the momentum summation with different choices of scattering rates. As shown in Extended Data Fig. 3, the results normalized by their high-temperature values are similar for $\Gamma_{140\text{ K}} = 35$ meV and 1 meV. The data presented in Fig. 1c use $\Gamma_{140\text{ K}} = 35$ meV.

We remark that the bonding band contribution is not included in our analysis. Although we do not expect qualitative difference between the bonding and antibonding bands for the temperature evolutions, we leave a detailed comparison for future studies.

Discussions on the entropy formula

In the following, we show that the formula $S = -k_B [f \ln f + (1-f) \ln(1-f)] \text{DOS}(E) dE$ can be justified in the presence of phase fluctuations under the assumption that such fluctuations are much slower than the electronic response time. Consider the Bogoliubov–de Gennes Hamiltonian with a frozen pattern of superconducting phase $\{\theta_{ij}\}$:

$$H = \sum_{ij,\sigma} t_{ij} C_{i\sigma}^\dagger C_{j\sigma} + \sum_{ij} \Delta_{ij} (e^{i\theta_{ij}} C_{i\uparrow}^\dagger C_{j\downarrow}^\dagger + \text{h.c.})$$

Here $C_{i\sigma}^\dagger$ creates an electron at site i with spin σ , t is the hopping integral, and Δ is the order parameter amplitude. H can be diagonalized after Bogoliubov transformation, $H = \sum_n E_n \gamma_n^\dagger \gamma_n$, where n labels the eigenstate, E_n is the eigenenergy, and γ_n is the eigen Bogoliubov operator. Since this is the problem of free Bogoliubov fermions in a fixed phase field, the entropy is given by $S(\{\theta_{ij}\}) = -k_B \sum_n [f(E_n) \ln f(E_n) + (1-f(E_n)) \ln(1-f(E_n))] = -k_B [f \ln f + (1-f) \ln(1-f)] \text{DOS}(E; \{\theta_{ij}\}) dE$. Note that here the dependence of E_n on $\{\theta_{ij}\}$ is absorbed into the DOS.

If the fluctuation of $\{\theta_{ij}\}$ is slow on the electronic time scale, the quench average in statistical mechanics can be used, namely, $S_{\text{measured}} = \langle S(\{\theta_{ij}\}) \rangle_p = -k_B [f \ln f + (1-f) \ln(1-f)] \langle \text{DOS}(E; \{\theta_{ij}\}) \rangle_p dE$, where $\langle \dots \rangle_p$ denotes the averaging using the Boltzmann weight $P(\{\theta_{ij}\})$ governing the thermal fluctuations of the phase field. By associating $\langle \text{DOS}(E; \{\theta_{ij}\}) \rangle_p$ with the ARPES-measured DOS, we arrive at the formula used herein.

Data availability

The raw data were generated at beamline 5-4 of the Stanford Synchrotron Radiation Lightsource and the Shen laboratory at Stanford University. The derived data supporting the findings of this study are available within the article and the Extended Data. Source data are provided with this paper.

35. Presland, M. R., Tallon, J. L., Buckley, R. G., Liu, R. S. & Flower, N. E. General trends in oxygen stoichiometry effects on T_c in Bi and Tl superconductors. *Physica C* **176**, 95–105 (1991).
36. Chen, S.-D. *High-Precision Photoemission Study of Overdoped Bi2212 Superconductors*. PhD thesis, Stanford Univ. (2021).

Acknowledgements We thank S.A. Kivelson, M. Sulangi, J.L. Tallon, and F.Wang for discussions, and J.L. Tallon for sharing the specific heat data. We thank J.-J. Wen, W. He, and Y.S. Lee for help with magnetic susceptibility measurements. Synchrotron ARPES measurements were performed at Beamline 5-4, Stanford Synchrotron Radiation Lightsource, SLAC National Accelerator Laboratory. The works at Stanford University and SLAC are supported by the US Department of Energy, Office of Science, Office of Basic Energy Sciences, Division of Materials Sciences and Engineering, under contract no. DE-AC02-76SF00515. The works at UC Berkeley and LBNL are supported by the US Department of Energy, Office of Science, Office of Basic Energy Sciences, Materials Sciences and Engineering Division under contract no. DE-AC02-05-CH11231 within the Quantum Materials Program (KC2202).

Author contributions S.-D.C., M.H. and Y.-F.L. performed the ARPES experiments. M.H., D.-H. Lu, S.-D.C., Y.H., J.-F.H. and Y.-F.L. contributed to instrument development. D.S., S.I., H.E.

and S.-D.C. prepared and characterized the samples. S.-D.C. analysed the data with input from T.P.D., J.Z., D.-H. Lee, and Z.-X.S. S.-D.C., M.H., D.-H. Lee and Z.-X.S. wrote the manuscript with input from all authors. Z.-X.S. supervised the project.

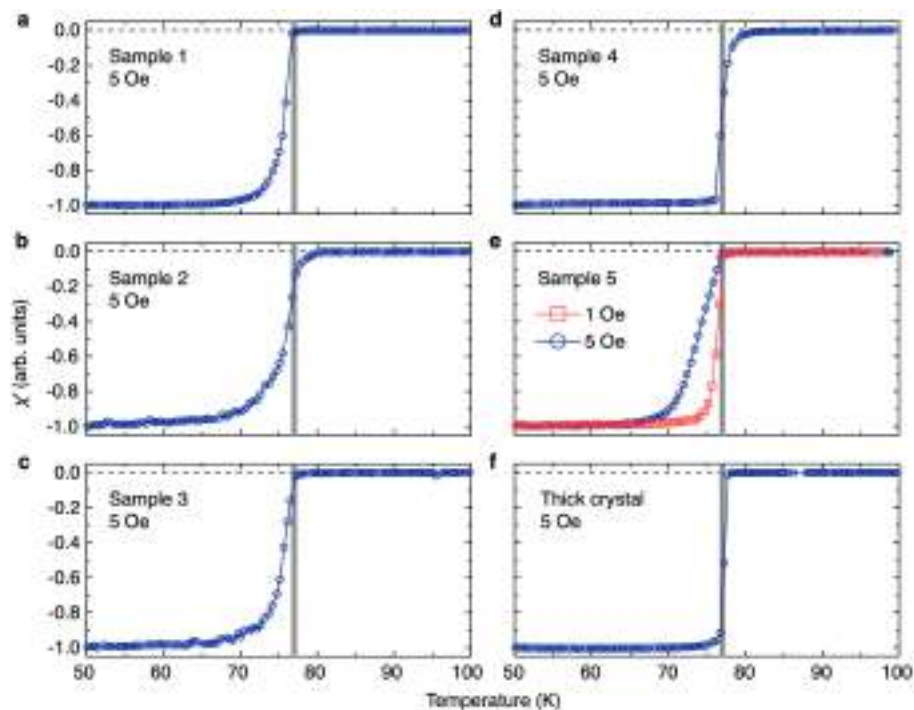
Competing interests The authors declare no competing interests.

Additional information

Correspondence and requests for materials should be addressed to Zhi-Xun Shen.

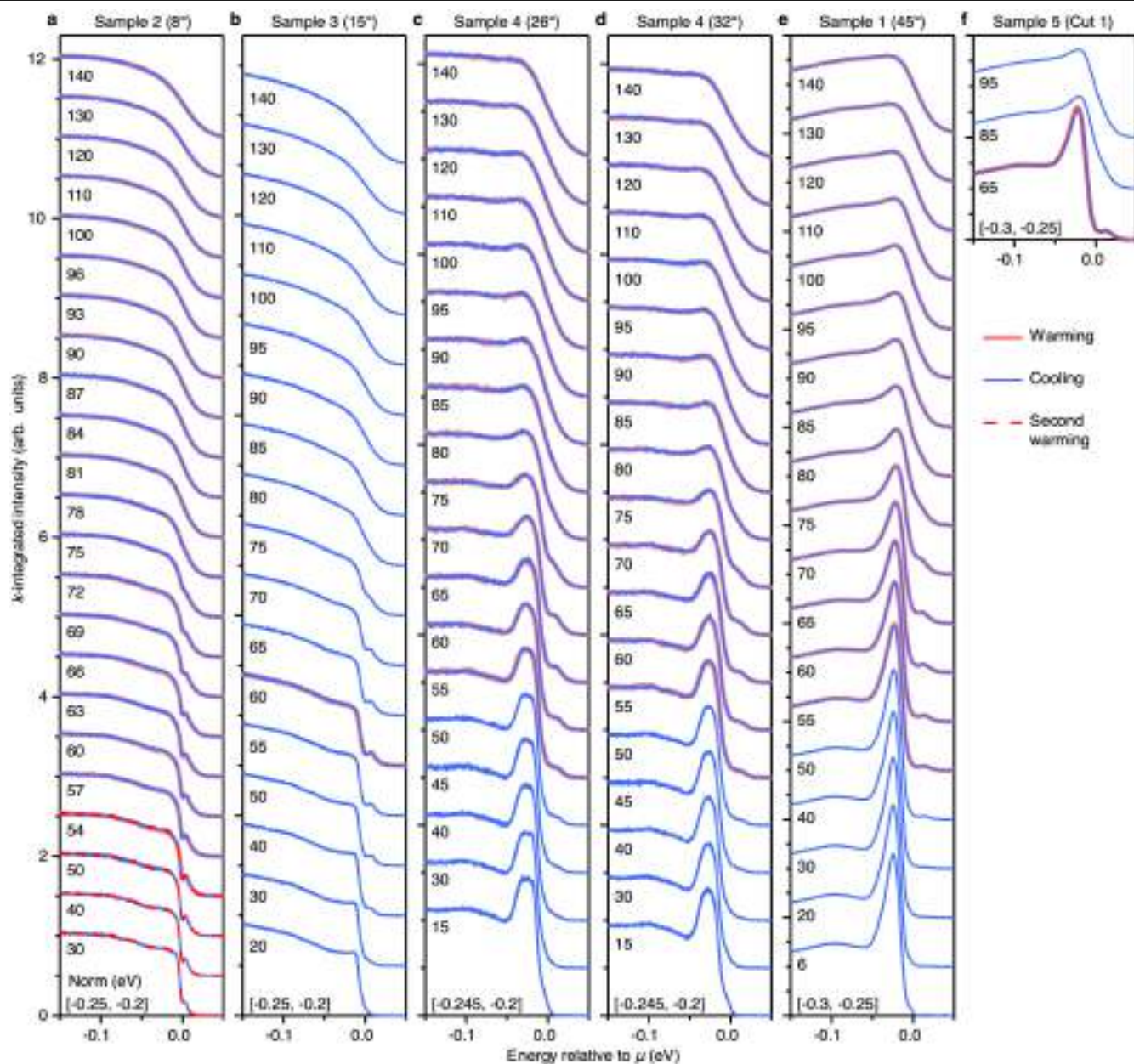
Peer review information *Nature* thanks the anonymous reviewers for their contribution to the peer review of this work.

Reprints and permissions information is available at <http://www.nature.com/reprints>.



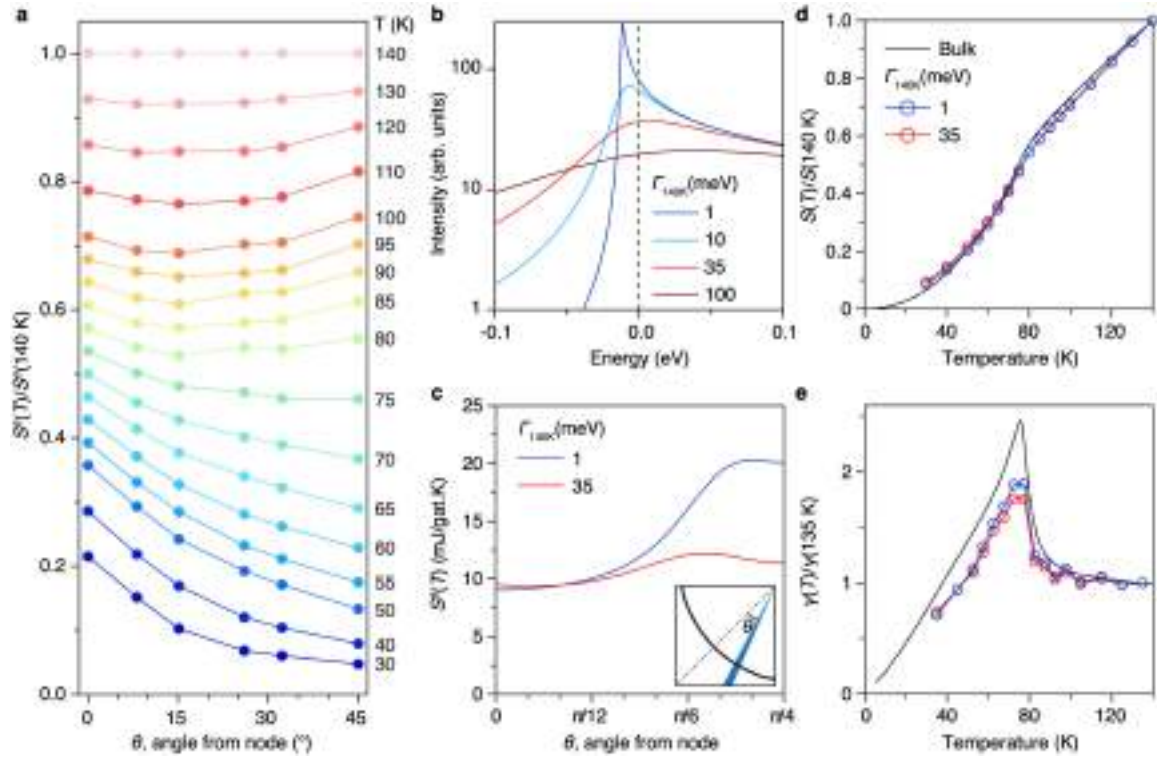
Extended Data Fig. 1 | Bulk characterization of T_c . **a–e**, Real part of the a.c. magnetic susceptibility (χ') for thin crystals exfoliated from the cleaved surfaces. The sample name and excitation field amplitude are marked in each

panel. The field frequency is 4 kHz. **f**, As in **a**, for a thick crystal. The grey lines in **a–f** mark $T_c \approx 77$ K.



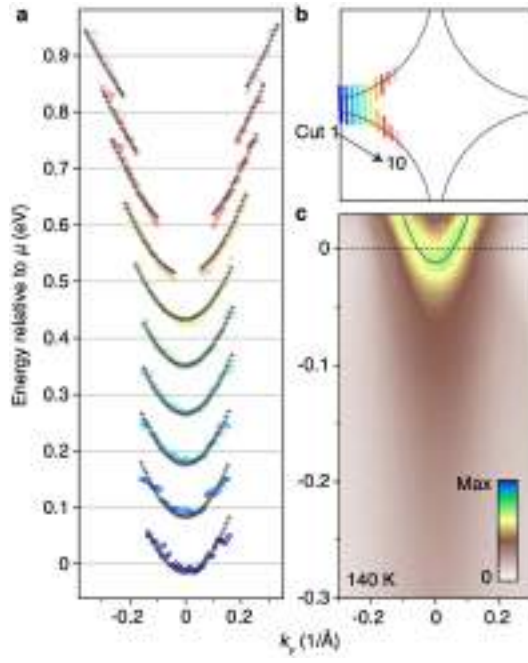
Extended Data Fig. 2 | Consistency of temperature scans. a-f, Momentum-integrated EDCs from temperature scans. The sample and cut location are marked on top of each panel (see also Extended Data Table 1). The y-axis tick increment is 0.5 for all panels. The curves are offset in steps of 0.5 (a-d) and 1 (e, f) for clarity, and the number beneath each set of curves represents the

temperature in K. Each EDC is normalized such that its average intensity equals 1 in the energy window given at the bottom of the corresponding panel. The consistency between curves measured during warming and cooling showcases the stability of the set-up and the absence of sample ageing effects.



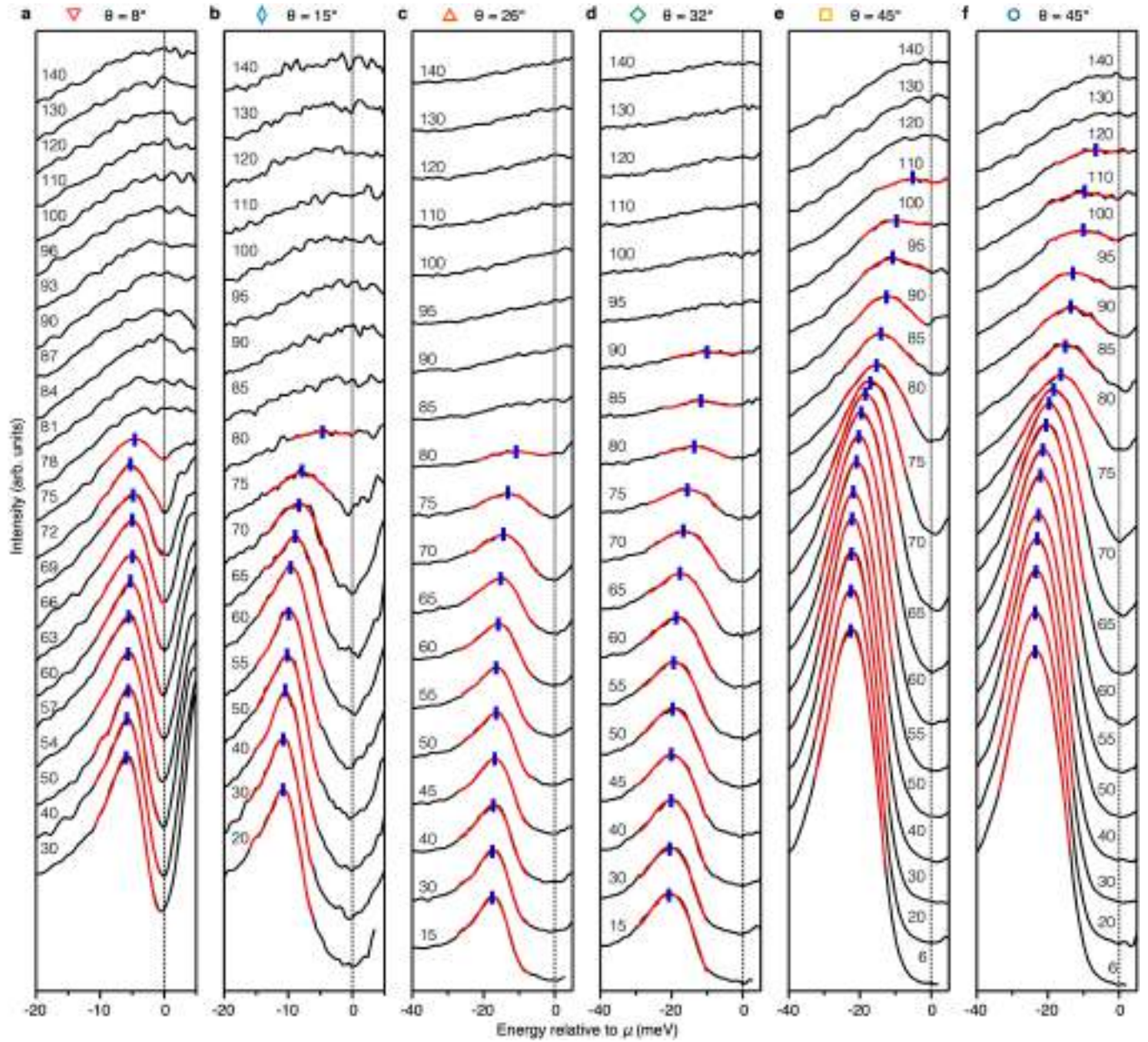
Extended Data Fig. 3 | Momentum summation. **a**, $S^\theta(T)/S^\theta(140\text{ K})$ plotted as a function of Fermi surface angle θ . We assume that $S^{\theta=0}(T) \propto T$. All the other data points are interpolated from the temperature evolutions shown in Fig. 1b. **b**, Spectral function of the antibonding band integrated along the Brillouin zone boundary. **c**, $S^\theta(140\text{ K})$ as a function of θ . Inset shows the tight-binding Fermi surface in the first quadrant of Brillouin zone. Curves in **b** and **c** are

calculated using an ARPES-determined tight-binding dispersion with different constant scattering rates. The antinodal scattering rate at 140 K is around 35 meV in our ARPES data. **d**, Temperature evolution of S calculated using data in **a** and **c**. **e**, Temperature dependence of γ obtained as the derivative of data in **d**. In **d** and **e**, the bulk results are plotted in black for comparison.



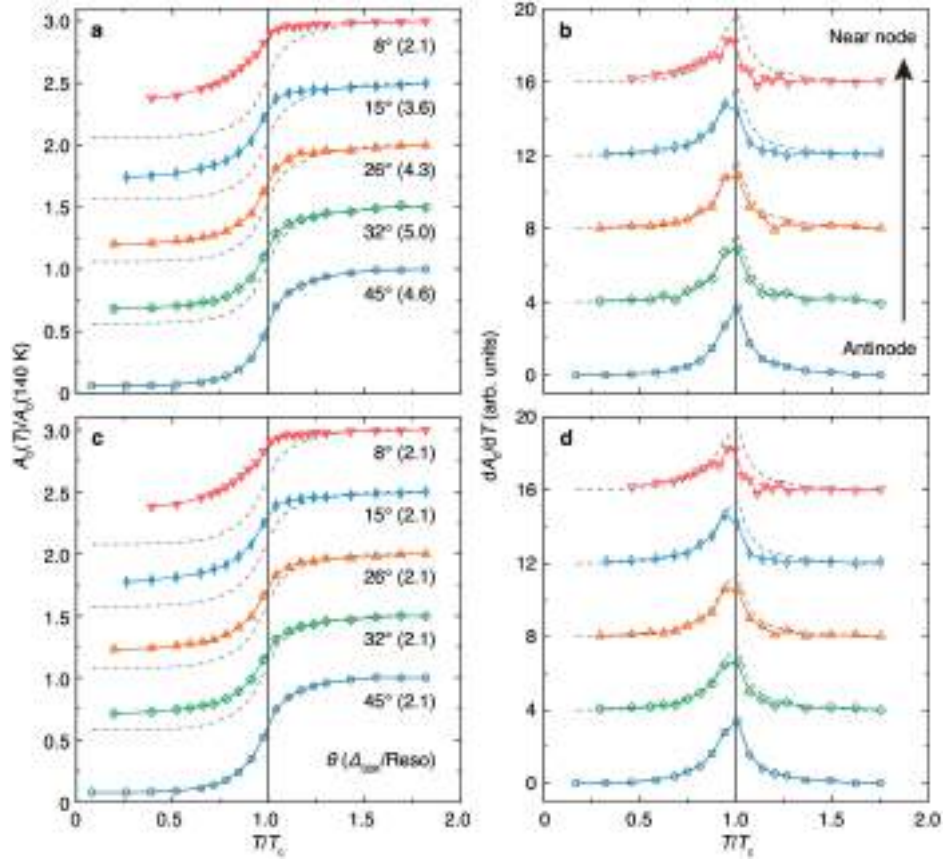
Extended Data Fig. 4 | Determination of the tight-binding parameters.

a, The dispersion of the antibonding band near the chemical potential (coloured circles) is extracted from ARPES data taken at 250 K on an overdoped Bi2212 sample with a slightly different doping ($p \approx 0.196$ from ref. ⁸). The temperature is chosen such that there are no gaps and more dispersion above the chemical potential can be identified. Data from different momentum cuts (as marked in **b**) are offset in steps of 0.1 eV for clarity. All data points are fitted at once to the tight-binding expression and the results are plotted as grey crosses. **b**, Momentum locations of data in **a** (coloured dots) plotted together with the antibonding Fermi surface (black curves) calculated from the fitting results. The black lines mark the first Brillouin zone. **c**, As in Fig. 2a, with the tight-binding dispersion plotted in grey. To compensate for the doping difference, we fix t_0 , t_1 , and reduce μ by 2.5 meV such that the Van Hove energy from the tight-binding model matches that of the OD77 ($p \approx 0.210$) sample studied in the text.



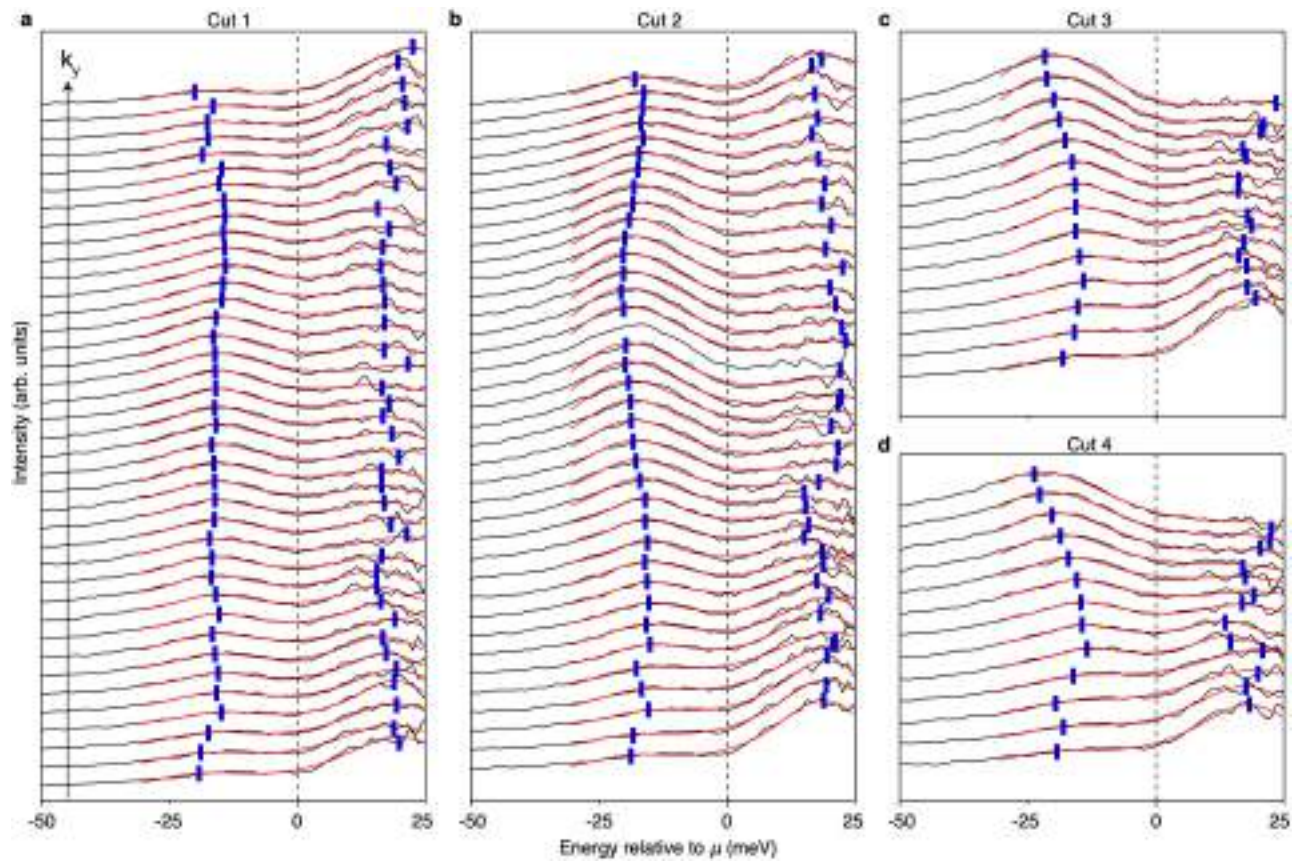
Extended Data Fig. 5 | Gap determination. a–f, k_F EDCs divided by the resolution-convolved Fermi function. The corresponding Fermi surface angle is labelled on top of each panel. The EDCs are offset for clarity and the number above each EDC marks the temperature in K. With minimal assumptions, we take the binding energy of the EDC maximum below the chemical potential

(vertical blue bars) as the gap size. For the procedure to be robust against noise, we first perform a polynomial fit to each EDC near its maximum (red curves) and then extract the energy position of the maximum from the fitted curve. With increasing temperature, we stop the analysis once the maximum shifts to zero energy.



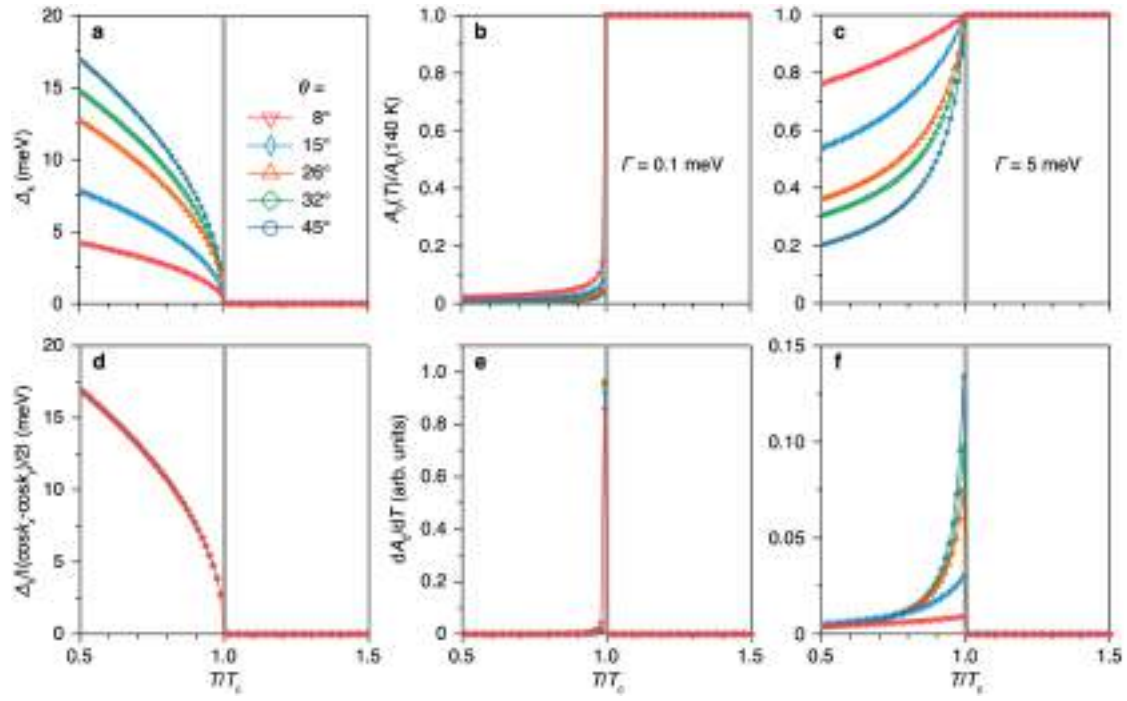
Extended Data Fig. 6 | Anisotropic gap filling and finite energy resolution.
a, b, As in Fig. 3c, d. The Fermi surface angle and the ratio between gap size at 30 K (Δ_{30K}) and energy resolution (Reso) are labelled beneath each curve in **a, c**, **d**, As in **a, b**, but obtained from data intentionally broadened in energy

such that all curves have the same Δ_{30K}/Reso of 2.1. The broadening is directly performed on data without Fermi-function division, such as those in Extended Data Fig. 2. The close resemblance between the top and bottom panels indicate that the anisotropic gap filling is not an artefact from finite resolution.



Extended Data Fig. 7 | EDC fitting for examining particle-hole symmetry. **a–d**, Fermi-function-divided EDCs along the blue curves in Fig. 4c. The cut number is labelled on top of each panel. Curves are offset according to their

k_y values for clarity. Each EDC is fitted using two Lorentzian peaks with identical width plus a constant background. The results are plotted in red, and the extracted peak positions are marked by the vertical blue bars.



Extended Data Fig. 8 | Spectral properties without phase fluctuations.

a, Expected temperature evolution of the superconducting gap for a pure d -wave superconductor in the mean-field theory, where T_c is set by gap opening. **b, c**, Simulated temperature evolutions of A_0 with different scattering rates Γ . The spectral function is calculated as $A(k, E) = (1 - \alpha)\Gamma / \{\pi[(E - E_k)^2 + \Gamma^2]\} + \alpha\Gamma / \{\pi[(E + E_k)^2 + \Gamma^2]\}$, where $E_k = \sqrt{\varepsilon_k^2 + \Delta_k^2}$, $\alpha = (1 - \varepsilon_k/E_k)/2$, and ε_k is the tight-binding bandstructure. **d**, As in **a**, with the gap sizes divided by their

corresponding d -wave form factors. **e, f**, Numerical derivatives of data in **b** and **c**, respectively. The vertical grey line in each panel marks T_c . Regardless of the choice of Γ , A_0 always stays constant for $T > T_c$ and shows a sharp drop across T_c with decreasing temperature. This singularity also shows up as a jump in the temperature derivative of A_0 . As such, the temperature evolutions of Δ_k , A_0 and dA_0/dT shown here are qualitatively different from those in Fig. 3.

Extended Data Table 1 | Details of each ARPES experiment

Sample	Data	Photon energy (eV)	Resolution (meV)	Temperature loop (K)
1	Fig. 1,2,3, $\theta=45^\circ$	19	5.0	55→140→6
2	Fig. 1,3, $\theta=8^\circ$	7	2.8	54→140→30→54
3	Fig. 1,3, $\theta=15^\circ$	7	3.0	60→140→20
4	Fig. 1,3, $\theta=26^\circ, 32^\circ$	7	4.1	55→140→15
5	Fig. 4	19	5.4	60→95→55